

Surface chemistry and electronics of semiconductor–nanosystem junctions I: metal-nanoemitter-based solar cells

H. J. Lewerenz · K. Skorupska · M. Aggour ·
T. Stempel · J. Grzanna

Received: 4 March 2008 / Revised: 25 July 2008 / Accepted: 29 July 2008 / Published online: 25 September 2008
© Springer-Verlag 2008

Abstract Photoelectrochemically prepared nanotopographies on semiconductors are used for realization of nanoemitter solar devices that are active in the photovoltaic and the photoelectrocatalytic mode. The development of solar devices by a nonlinear electrochemical process and combined chemical/electrochemical metal deposition is described. Based on this low-temperature scalable approach, first efficiencies of 7.3% in the photovoltaic mode are reported for the photoelectrochemical solar cell n-Si/SiO₂/Pt/I₃⁻Γ⁻. With p-Si/Pt nanocomposite structures, light-induced H₂ evolution is achieved. The surface chemistry and morphology is analyzed by photoelectron spectroscopy (PES), Fourier transform infrared spectroscopy, and high-resolution scanning electron microscopy. The operational principle of Pt-based nanoemitter solar devices that use silicon single crystal absorbers is analyzed by Mott–Schottky plots, chronoamperometric profiles, and PES. Related to simultaneous oxide formation during Pt deposition, evidence for the

formation of a metal–oxide–semiconductor junction is obtained that explains the observed electronic behavior.

Keywords Solar energy · Silicon · Nanostructure · Wet processing · Electrochemistry

General introduction to parts I and II

The nano-dimensioned semiconductor systems presented in part I and part II are (1) metal nanoemitters formed on Si and (2) proteins immobilized on a nanostructured (so-called step-bunched Si) and a layered semiconductor. Both systems are characterized by nano-dimensioned particles that are attached to semiconductor surfaces. Another common feature relates to the description of the electronic and energetic properties which is done here using concepts from applied semiconductor physics such as, for instance, that of metal–oxide–semiconductor (MOS) or metal–insulator–semiconductor junctions [1]. Although such common traits in the nano-dimensionality of the used adsorbates and their interfacial behavior with nanostructured semiconductor substrates which connect the—at first glance—rather differently appearing nanocomposite systems clearly exist, there is also a conceivable difference in the underlying science of solar energy conversion devices and of proteomics. Therefore, we have decided to represent each system separately.

The first article treats the surface chemistry and electronic properties of semiconductor nanosystems with deposited metallic islands that function as emitters in nanocomposite solar energy converting devices. The device efficiency strongly depends on electronic properties which, in turn, are largely determined by the surface or interface chemistry at the rectifying junction. Therefore, surface

Contribution to the Fall Meeting of the European Materials Research Society, Symposium D: 9th International Symposium on Electrochemical/Chemical Reactivity of Metastable Materials, Warsaw, 17th–21st September 2007.

H. J. Lewerenz (✉) · K. Skorupska · T. Stempel
Interface Engineering Group, Division of Solar Energy,
Helmholtz Zentrum Berlin,
Berlin, Germany
e-mail: lewerenz@hmi.de

M. Aggour
Faculty of Science, Tofail University,
Kenitra, Marocco

J. Grzanna
Department FMD, Helmholtz Zentrum Berlin,
Berlin, Germany

analytical methods and electronic characterization are used for analysis.

In the second article, a review is given on our work on nano-dimensioned soft-matter molecules, i.e., proteins, adsorbed at semiconductor surfaces. Very little is known about electronic properties of protein-semiconductor contacts. Scanning probe microscopy experiments including scanning tunneling microscopy (STM) and tapping mode atomic force microscopy are employed for the analysis of the semiconductor/protein/metal STM-tip system.

Introduction

The preparation of nanoemitter solar energy converting structures, described below, is based on self-organized (photo)electrochemical processes that are correlated with distinct nanotopographic surface changes. Such self-organized processes are ubiquitous in nature and have attracted considerable attention over decades [2–4]. Presently, with the advent of nanotechnology, successive miniaturization demands advanced tools in preparation. Two major routes can be discerned: (1) chemical and electrochemical preparation of nanosystems (carbon, WO_3 , TiO_2 nanotubes, colloids and photonic crystals, for instance [5–9]) that involves some self-organization or self-assembly aspect and (2) externally directed fabrication of such structures by optical and electron beam lithography or by focused ion beam etching, for example [10, 11]. The latter processes, although reaching almost the resolution of the chemical/electrochemical approaches in combining the methods [11], will have to fulfill the demands on upscaling of nanostructures for large area applications. Presently, this can be better realized in systems that show self-organization or self-assembly properties. This is particularly important in solar energy conversion applications where large areas for the absorber component of solar cells are needed, but it is also true for the fabrication of biological sensors [12, 13], for instance.

In this article, we follow the chemical/electrochemical approach. A route towards the development of silicon-based photoactive devices is described. The devices are shown to operate in the photovoltaic and photoelectrocatalytic mode. Device structures consist of metallic nanoemitters as light-induced minority carrier charge collecting component of a solar cell embedded in a passivating surface layer on top of the semiconductor absorber.

Experimental

Electrochemical experiments have been performed in the standard three-electrode potentiostatic arrangement using Pt

counter and saturated calomel (SCE) or Ag/AgCl reference electrodes. Solutions were prepared from the highest available purity chemicals (reagent grade or ultrapure) and ultrapure water (18 $\text{M}\Omega$). In the experiments on Si, solutions were deaerated by N_2 purging (5N-grade). The experimental arrangement for in situ Fourier transform infrared spectroscopy is given in [14]. Light-to-electricity conversion experiments were done in the experimental electrochemical cell that was also used for the electrochemical processing of the silicon substrates. Illumination was provided by a W-I lamp. N-type Si (111) with a doping level of $4 \times 10^{15} \text{ cm}^{-3}$ and p-type Si(100), doped $5 \times 10^{14} \text{ cm}^{-3}$ were used. The nominal miscut was 0° .

Results and discussion

The section contains: (1) a short summary of the theoretical model regarding oscillatory phenomena at silicon electrodes, (2) the description of the (photo)electrochemical preparation of photoactive devices, and (3) an overview of the silicon surface chemistry after Pt electrodeposition. A more detailed analysis of the surface chemistry, analyzed by synchrotron radiation photoelectron spectroscopy, is given in this volume in the article of K. Skorupska.

Electrochemical self-organization at Si surfaces

Silicon (photo)electrochemistry is characterized by several phenomena such as porous Si formation [15–17], metastable topographies [18, 19], step-bunching [20, 21], electropolishing [22, 23], photonic crystal fabrication [24], and oscillatory behavior [25–28]. First, an overview of the (photo)electrochemistry of Si is given (Fig. 1). The schematic in Fig. 1

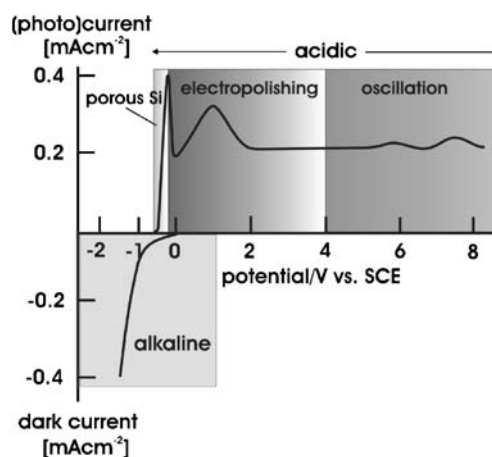


Fig. 1 Photo- and dark current–voltage branches of n-Si in acidic-fluoride-containing solution (anodic branch) in dilute NH_4F solution at pH 4 and in alkaline solution (cathodic branch) for preparation of oxide nanopores and step-bunched surfaces, respectively

shows the combined behavior in acidic (anodic current branch) and in alkaline (cathodic current branch) electrolytes. In the former, the onset of current oscillations is observed at about 5 V. They are used for the preparation of photoactive devices (see “Solar devices”). The cathodic branch of Fig. 1 shows the potential region in which so-called step-bunched surfaces, characterized by large atomic terraces and step heights in the order of 10–15 atomic bilayers of individual height of 0.314 nm, are prepared. Because of their unique structural and electronic properties [20, 21, 29, 30], these surfaces can also be used for protein adsorption (see part II).

For the development of solar cells by low-temperature scalable processes, the structural features that occur in the anodic oxide on silicon during photocurrent oscillations are used as template for metal nanoemitter deposition. The presence of an oxide at Si surfaces during oscillation has been shown by photoelectron spectroscopy and in situ Fourier transform infrared spectroscopy (FTIR) measurements [31]. The oxide thickness varies periodically displayed in Fig. 2. The variation of the signal of the asymmetric Si–O stretching mode yields oxide thicknesses between 17 and 27 monolayers (ML). The average integral oxide thickness is 22 ML. Using a value of 0.45 nm for one ML (Schmeißer D, private communication), the resulting oxide thickness d_{ox} varies between ~7.7 and ~12 nm. The current, however, shows a modulation depth of >90% despite a minimum oxide thickness of almost 8 nm where the oxide should be electrically insulating. Native oxides on silicon are already insulating at a considerably smaller thickness of 1.2–1.5 nm, for instance. Therefore, a mechanism had to be postulated by which a rather small change in mean oxide thickness (± 5 ML) on a background of a 10-nm-thick oxide layer (corresponding to the average oxide thickness of 22 ML during oscillations) produced the observed large current modulation. In our initial work, this

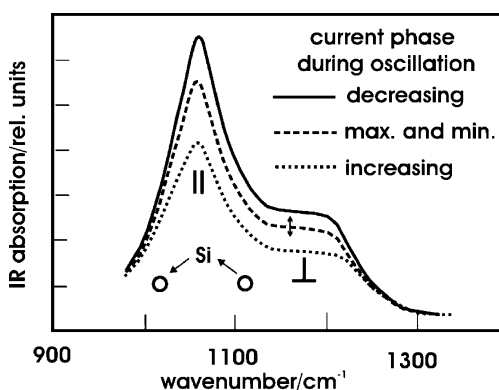
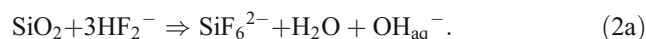
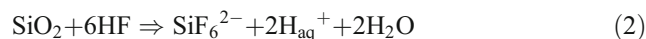
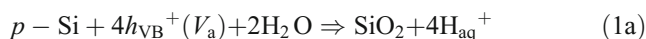
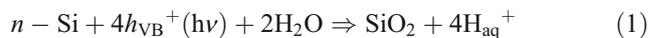


Fig. 2 Fourier transform infrared spectroscopy for in situ determination of silicon oxide thickness during photocurrent oscillations at n-Si (111) electrodes in 0.1 M NH₄F, pH 4; the asymmetric Si–O stretching mode is displayed for three conditions as indicated; the perpendicular and parallel vibrational modes are labeled accordingly

led to the postulation of electrolytically conducting channels within the anodic oxide [32] before such pores have actually been observed. The concept is schematically shown in Fig. 3a where these channels are represented as pores. The opening (process 2) and closing (process 1) of these pores can affect the photocurrent (n-Si) due to the efficient minority carrier collection at these sites. Subsequent experimental and theoretical work (see below) showed that the closing process is related to new oxide formation at the bottom of the respective pore. This efficiency of the carrier collection results from the large diffusion length (>100 μm) in single crystalline Si (see Fig. 3b for visualization), and this operation principle has also been used earlier in the development of point contact solar cells for concentrator applications [33]. Basically, the current modulation during oscillations can be qualitatively explained by this behavior, but for the occurrence of sustained oscillations, further assumptions have to be made that relate to their physico-chemical origin to and the nature of the feedback mechanism.

Below, the model that we have developed earlier is shortly reviewed [25–28]: It is based on the light-induced anodic oxide formation at n-Si (or bias-induced oxidation of p-Si) and on the simultaneous etching in HF and HF₂[−] (dilute NH₄F solutions). This dynamic competition is described in the model by the temporal behavior of so-called oxide thickness oscillators where the cycle time of the thickness oscillators defines the temporal evolution of the system. The oxidation (Eqs. 1, 1a) and etching (Eqs. 2, 2a) reactions are



Here, h_{VB}^+ indicates holes from the valence band and $h\nu$ symbolizes the light-induced oxidation process; for p-Si, oxidation occurs via an applied anodic potential (V_a). Etching by the hydrogen-bridge complex HF₂[−] only takes place at moderately acidic pH. It has to be taken into account in our experiments in dilute NH₄F solutions (0.1–0.2 M) at pH 4.

The initial oxidation takes place at a bare H-terminated Si surface [34]. Since the oxidation is very fast, as shown in Fig. 4, the cycle time of the thickness oscillators is given predominantly by the oxide thickness and the etching period of the formed oxide which is considerably slower than the formation time. The oscillating photocurrent (on

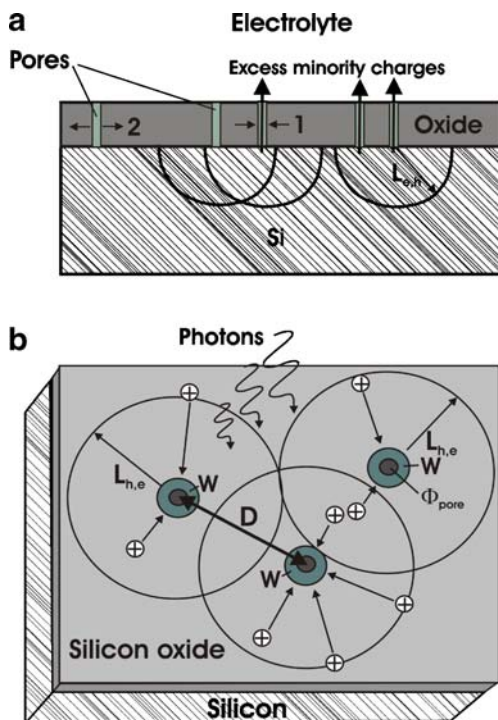


Fig. 3 Schematic of the fluctuating pore model. **a** Side view of electrolytically conductive channels in the oxide which allow excess minority carrier collection through such pores. **b** Top view showing the (idealized) geometry of the concept with pore diameter Φ_{pore} , depletion layer width W , and minority carrier diffusion length L_c (p-Si) and L_h (n-Si)

n-Si) and the dark current (p-Si) are derived from an initial current peak $J_i(t)$, resembling the experimental behavior in Fig. 4 and a temporal evolution sequence that is based on a combination of probability theory and Markov processes [25]. The oscillating current $j(t)$

$$j(t) = \sum_i \int_{t_i^{\min}}^{t_i^{\max}} p_i(\tau) J_i(t - \tau) d\tau \quad (3)$$

is related to the synchronization function $p(t) = \sum_i p_i(t)$ where the $p^i(t)$ are derived by a Markov chain [35]. The synchronization state in the i th cycle is then defined by previous synchronization state $p^{i-1}(t)$ in the following way:

$$p_i(t) = \int_{t_{i-1}^{\min}}^{t_{i-1}^{\max}} p_{i-1}(\tau) q_{i,\tau}(t - \tau) d\tau. \quad (4)$$

Here, $q_{i,\tau}$ is the probability distribution of the cycle time of the thickness oscillators starting the i th cycle at the time τ . Figure 5 shows a “train” of p_i together with the $q_{i,\tau}$ for an etching process of an earlier formed oxide within one cycle (labeled τ) and of a later formed one (τ^*). The different time intervals indicate that the earlier formed oxide with a longer “lifetime” etches slower than the later formed one, which is expressed by the different intervals related to τ and τ^* . The reasons for this assumption are schematically

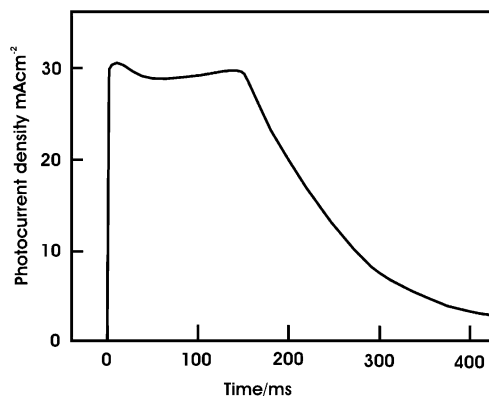


Fig. 4 Time-resolved current measurement using an oscilloscope of the initial oxidation of n-Si(111) in dilute NH_4F at pH 4 for an anodic potential of 6 V (SCE) and illumination with a W-I lamp by opening a shutter; only the first oxidation phase is shown in which approxi-

represented in Figs. 6 and 7. First, we inspect the situation of the growing oxide on a bare silicon surface as shown in Fig. 6a,b. The side view in Fig. 6a shows initially formed oxide islands which, due to the volume mismatch of 2.27 (oxide vs. Si), grow into the substrate but also extend towards the exterior of the geometrical surface. It is well known from microelectronics that the oxide is under compressive stress, whereas Si is under tensile stress [36]. The top surface view in Fig. 6b shows the situation at a more advanced stage of the oxidation process. We use the terminology of oxide I and II to characterize those oxides that have been formed at earlier stages of the process (I) and that are assumed to be more homogeneous in composition than later formed oxides (II) which are formed by oxidation of the considerably stressed Si substrate. In Fig. 6b, the successive oxidation process of the surface within the initial cycle is indicated by the areas that are located between oxide I islands. At an advanced stage of the oxidation process, the silicon substrate is under tensile stress underneath the oxide and under compressive stress

synchronization state

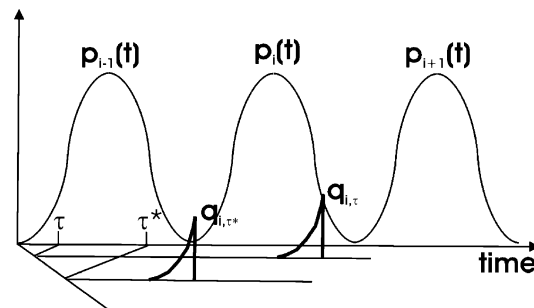


Fig. 5 Visualization of the mathematical process described in Eq. 1 showing the synchronization states $p_i(t)$ and the probability distribution of the periods of the oxide thickness oscillators $q_{i,\tau}$. The influence of the contraction of the time interval for later formed oxides that etch faster is indicated by the starting time τ^* (see text)

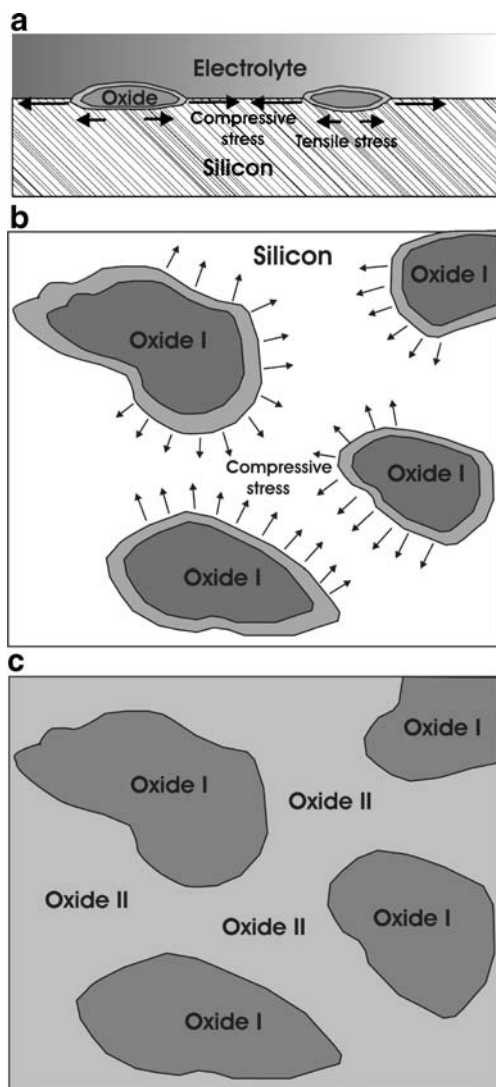


Fig. 6 Schematic of the influence of volume mismatch between Si and its oxide on the stress in the two materials. **a** Side view for the initial oxidation of a bare silicon surface. **b** Top view indicating that initially grown oxides (oxide I) exert compressive stress into the intermediate (uncovered) areas of silicon. **c** Formation of oxide II in increasingly stressed Si substrates during oscillatory behavior (where the surface is always covered with silicon) which results in a fast three-dimensional etching behavior of oxide II (see text)

between the oxide islands, as indicated by the arrows in the figure. From fractal photocorrosion of Si, it is known that dissolution and oxidation are favored at sites with stress-induced distortion of bonds [37]. Then, the later formed oxide II will contain considerably more defects such as micro- and nanocracks that eventually can develop into nanopores which allow electrolyte transport to the Si surface (Fig. 6c). Accordingly, this defectuous oxide will etch faster due to three-dimensional etching around pores compared to a more layer-type etching of oxide I.

In Fig. 7, the influence of the faster etching of oxide II is schematically shown. We have depicted a situation in which

the later formed oxide II of cycle 1 (Fig. 7a) is etched faster than oxide I. Figure 7b shows the situation where oxide II has been etched away and underneath, the new oxide I is formed in the subsequent cycle 2. This new oxide I is formed in the initial stage of cycle 2, of better structural quality (lower defect density), and hence etches slower. Figure 7a shows schematically that at the position where the former defect-rich oxide was formed, a new defect-poor oxide grows. For better visualization, the oxides of type I from the earlier cycle 1 are shown as rather thick islands, although at the time when oxide I is formed in the subsequent cycle 2, they should have been largely dissolved. This overall behavior results in a contraction of the probability distribution of the cycle times for the thickness oscillators for later formed oxides, as shown in Fig. 5. The subsequent synchronization state retains its original shape due to this contraction, resulting in sustained oscillations. Under these conditions, the Si oxide is located in two neighboring cycles only [38]. Damped oscillations occur if the etching time interval of successively formed oxides does not contract enough. It should be noted that this oscillatory behavior is a macroscopic phenomenon, meaning that synchronization occurs throughout the sample, and accordingly, any structure formed in this process exists on

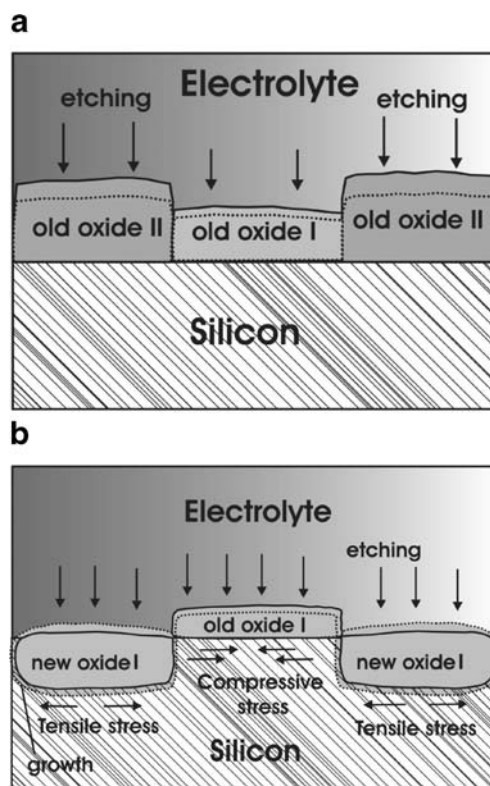


Fig. 7 Schematic side view of synchronization by etching. **a** The earlier formed oxide I and the later formed oxide II which etches faster (see dotted lines). **b** Situation in which oxide II has been completely etched and new oxide I of the next cycle is growing

the overall sample surface, resulting in the scalability of the related nanostructures.

Figure 8 shows high-resolution scanning electron micrographs of Si samples that were immersed at a phase of the current where the oxide thickness, as determined from FTIR measurements, was thinnest. Nanopores on both, n-Si and p-Si, are clearly visible. Pore sizes are in the range of 10–30 nm on n-Si and about 50 nm on p-Si. In addition, the pore density is considerably different on both samples; for p-Si, a much lower density and larger pores are found. This might in fact point to the existence of current bursts on such samples [39] because the anodic potential drop for p-Si occurs almost exclusively across the interfacial oxide due to the accumulation layer formed upon anodization.

Solar devices

Solar energy converting structures using the self-organized nanopore structures shown in Fig. 8 can be realized by

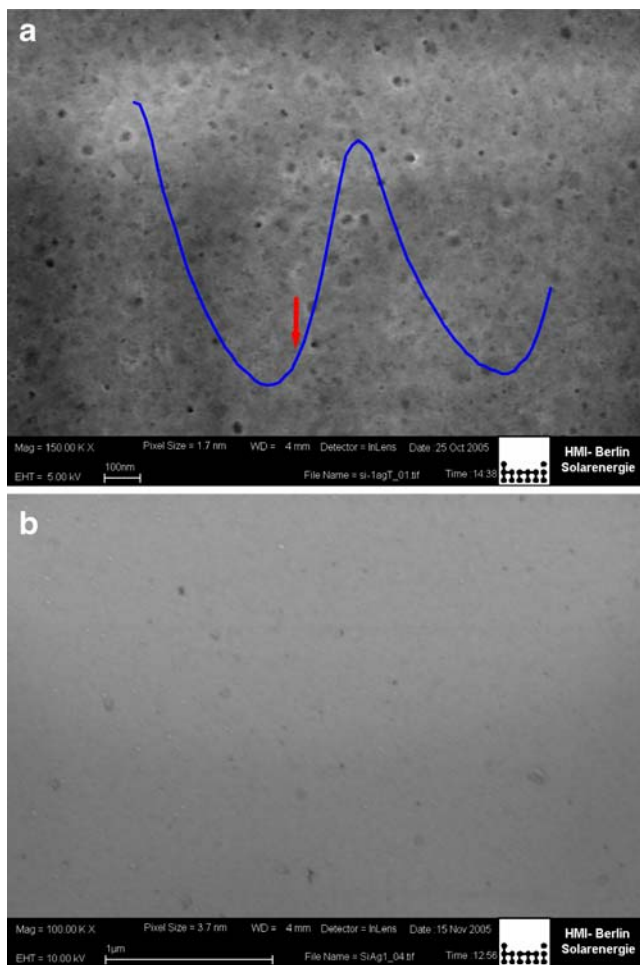


Fig. 8 High-resolution scanning electron microscopy (HRSEM) images of Si samples immersed at the increasing branch of the oscillating current. **a** n-Si(111), **b** p-Si(111); oscillatory conditions: +6 V (SCE), dilute NH_4F , pH 4

electrodeposition of metallic islands into the pores. Electrodeposition will only take place at those pores that have electrical contact with the Si substrate. If the remaining oxide outside the pores is electrically insulating, the electrodeposition process itself produces spatially selective metal deposition. For solar energy conversion devices, three operational modes can be discerned: (1) solid-state photovoltaic operation, (2) light-to-electricity operation in photoelectrochemical solar cells (PECS) that employ redox electrolytes, and (3) photoelectrocatalysis application. For (1), the metal has to form a rectifying junction with silicon, for (2), the redox electrolyte has to be selected such that a large contact potential difference between the redox potential and the Si Fermi level exists, and for (3), the contact potential between the catalytic reaction and the Si Fermi level must be large and metals with catalytic activity for the respective reaction (for instance Pt in case of light-induced H_2 evolution) have to be chosen.

Figure 9 shows a scheme how to realize a nanoemitter solar device where the pores in the oxide have been deepened into the Si substrate by alkaline etching. Subsequently, the voids are filled with metallic emitter materials for enhanced collection of minority carriers, generated by low-energy photons deeper in the silicon absorber. We focus here on the realization of PECS that operate in the photovoltaic mode because of their facilitated preparation compared to solid-state devices that need a transparent conductive front material to collect the light-induced minority carriers. In addition, in the case of PECS, the metal nanoislands do not necessarily have to form a Schottky barrier with Si because the electrochemical potential of the redox electrolyte defines the contact potential difference with Si.

A complication that reduces the photovoltage and thus the conversion efficiency considerably, however, is the influence of so-called metal-induced gap states (MIGS) [40] which are known to result in Fermi level pinning. Fermi level pinning is known since long in semiconductor devices [1] and describes the independence of the barrier height in Schottky junctions on the contacting metal's work function. We will see below that due to the specific conditions for Pt deposition, Fermi level pinning is not observed in this case.

Pt electrodeposition is well established [41], and in PECS, the contact potential difference is given by $E_F(\text{Si}) - E_{\text{Redox}}$. In iodine–iodide redox electrolyte, this difference is approximately $4.2 \text{ eV} (E_F(\text{Si})) - 5.1 \text{ eV} (E_{\text{Redox}}(I^-/I_3^-)) = -0.9 \text{ eV}$ (using a value of 4.6 eV for the work function of the reversible hydrogen electrode; accordingly, the work function of the SCE is at 4.86 eV); hence, a considerable photovoltage can be expected. For photoelectrocatalytic operation, Pt can be photo-deposited into the nanopores of p-Si samples after emersion from the fluoride containing electrolyte where current oscillation

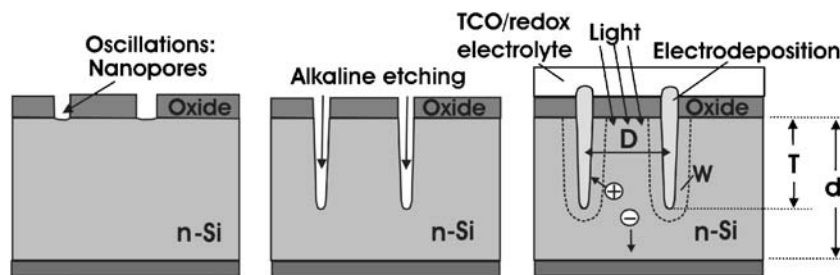


Fig. 9 Concept for a nanoemitter solar cell and its preparation. *Left:* nanopores are electrochemically formed in silicon oxide; *middle:* deepening of these pores by alkaline etching which selectively attacks silicon; *right:* filling of pores with an emitter material that forms a

Schottky junction with Si, contacting the emitter with a TCO (transparent conductive oxide) or a redox electrolyte for solid-state or photoelectrochemical solar cells, respectively; labeling of the geometric parameters follows Eqs. 5 and 6

occurs. Such device can then be employed, for instance, for light-induced proton reduction to H₂.

The optimum performance of the nanoemitter device involves conditions concerning the minimum distance between the nanoemitter islands in relation to the excess minority carrier diffusion length $L_{h,e}$ (for holes and electrons, respectively) of the semiconductor. From simple geometric considerations on the overlap of the circles for L in Fig. 3b, the horizontal nanoemitter distance D is defined by

$$D \leq \sqrt{2}(L_{h,e} + W + r_{em}) \tag{5}$$

where W is the semiconductor depletion layer width and r_{em} the radius of the metallized pore. Perpendicular to the geometric surface, the inequality

$$d_{\perp} \leq T_{pore} + W + \frac{L_{h,e}}{2} \tag{6}$$

must hold for efficient cells (see Fig. 9); here T_{pore} denotes the depth of the metallized pores which can be extended from the oxide into the Si substrate by alkaline etching as indicated in Fig. 9. The variation of the distances D and d_{\perp} will allow adjustment of the efficient carrier collection in low electronic quality material that is characterized by a small minority carrier diffusion length by decreasing the lateral distance between the nanoemitters. Hence, this concept provides, in principle, high solar energy conversion efficiencies by adjusting the nanoemitter distance and depth.

Figure 10 shows the electrodeposition protocol for Pt. At a potential of -0.8 V (SCE), the sample was held for 60 s. The dark current i_D (n-Si is in accumulation under these conditions) shows a time dependence close to $i_D = t^{-1/2}$ which is well known for a diffusion-controlled reaction that shows Cottrell-type behavior [42]. The overall accumulated charge reaches 13 mCcm^{-2} which, for a four electron reduction process of the PtCl_6^{2-} anion, would correspond to about 20 ML deposited metal. Two additional aspects, however, have to be taken into account: the I–V characteristic for Pt deposition (not shown) shows that the process occurs on top of underlying H₂ evolution which amounts to a factor of ~ 0.4 of the overall charge in the reaction.

Accordingly, the amount of deposited Pt reduces to ~ 12 ML. In this consideration, increased hydrogen evolution due to the catalytic activity of Pt, which would further reduce the amount of deposited Pt, is not considered because it is difficult to assess. Secondly, the Pt deposition potentials are energetically located at $+0.54$ and $+0.71$ V (SCE), i.e., below the Si valence band edge. Therefore, hole injection into the valence band with subsequent Pt deposition can occur [43, 44]. It is presently not known how these stepwise reduction processes from Pt^{4+} to Pt^{2+} and to Pt^0 from the valence band electrons compete with the conduction band reduction process. The occurrence of the distinct reduction peak in Fig. 10, however, indicates a conduction band reaction where the high electron concentration in the accumulation layer contributes efficiently to the metallization of the nanopores. In general, a correlation between deposition charge and metal island size and distribution is yet difficult to make, and this topic needs further investigation. Recently, evidence for the contribution of surface states in the electrodeposition process has been obtained (Stempel et al., manuscript in preparation).

The result of the metal deposition process is shown in the high-resolution scanning electron micrograph of Fig. 11. It can be seen that not all pores are filled with Pt

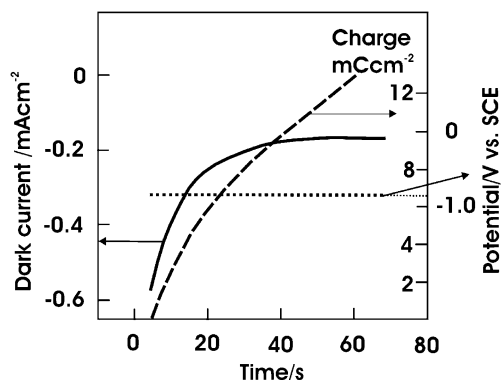


Fig. 10 Protocol for electrodeposition of Pt from a solution of 1 mM PtCl_6^{2-} , 0.1 M K_2SO_4 , pH 3.8; the potential, dark current, and charge are displayed for an n-Si/oxide system

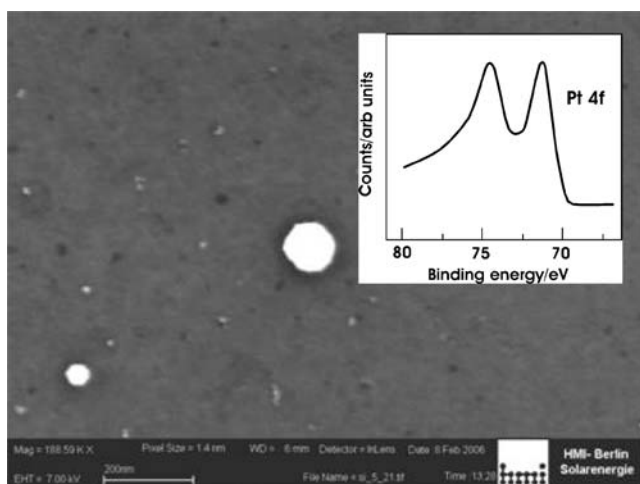


Fig. 11 HRSEM image of metallized oxide nanopore surface where the Pt islands, in part having overgrown the pores, are seen by the material contrast; note that not all pores are filled (see text); the *insert* shows an XPS result on the metallized surface with the Pt 4f line, excitation by $MgK\alpha$ (1256 eV)

that is visible due to the enhanced material contrast. The partial pore filling is attributed to the fact that during oscillations, not all pores have electrical contact to the Si substrate because they are in different phases of their growth. In addition, some pores appear to have been overgrown, reaching Pt diameters close to 100 nm. The insert of Fig. 11 shows an X-ray photoelectron spectrum (XPS) of the Pt 4f_{7/2-5/2} line demonstrating that Pt is indeed found on the surface and that its oxidation state, given by the core level binding energy of 71 eV, corresponds to elemental Pt⁰.

Figure 12 gives the output power characteristic of a device with Pt islands in iodine–iodide redox electrolyte. A conversion efficiency of 7.3% is reached. Since high-quality single crystalline Si substrates have been used, it is expected that this efficiency will increase once the losses in the system are assessed and eliminated. Presently, we

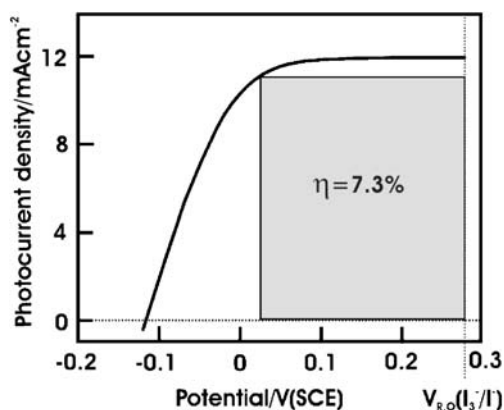


Fig. 12 Output power characteristic of a photoelectrochemical solar device with n-Si operating in the photovoltaic mode; electrolyte 50 mM I₂, 0.1 M KI; light intensity 37 mWcm⁻² (W-1 lamp)

consider interface recombination [45] at the Si/SiO₂ boundary at the local Si/Pt contacts and problems with oxide quality (trapped charge) as most deleterious. The data in Fig. 12 show that as predicted, the system adjusts to the Fermi level of the redox couple. In different experiments, it was shown that linear Mott–Schottky plots are obtained (Stempel et al., manuscript in preparation). This demonstrates that external biasing modulates the depletion (space charge) layer and contradicts the assumption of a prevalent influence of MIGS. The relatively small contact area between Pt nanoislands and Si and/or a thin interfacial oxide layer can be responsible for the absence of Fermi level pinning. The latter would reduce the spatial overlap of interpenetrating evanescent metal states into the semiconductor. In “Basic interfacial chemistry analyzed by photoelectron spectroscopy”, the surface chemistry after Pt deposition is considered, demonstrating Si oxidation in the process.

In Fig. 13, first results on light-induced H₂ evolution are presented for p-Si. The onset of the photoelectrocatalytic reaction is observed at $V = -0.05$ V (SCE), i.e., ~ 0.2 V positive of the equilibrium potential for the hydrogen evolution at the pH of the 0.05 M H₂SO₄ solution. Separate experiments show that saturation of the photocurrent occurs at considerably more negative potentials at about -2 V (SCE) where currents reach 12 mAcm⁻² (Stempel et al., manuscript in preparation). The sluggish current increase observed here indicates recombination and possibly current transport losses. In addition, the contact potential difference between the hydrogen evolution reaction and the Fermi level position of p-Si is only about 0.4 V if semiconductor physics data (electron affinity, doping level, energy gap) are compared with the work function of the normal hydrogen electrode (~ 4.6 eV). This reduced contact potential difference is accompanied by a rather small band bending, and surface/interface recombination can then dominate the behavior. Here, too, optimization of the various interfaces and of the metal deposition process is necessary to produce

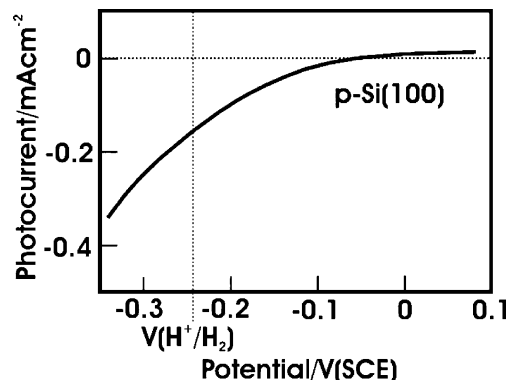


Fig. 13 I–V characteristic showing the photoelectrocatalytic activity of the Pt/SiO₂/p-Si/H⁺–H₂ device (see text)

more efficient devices. It is more promising for photoelectrocatalytic applications, however, to use semiconductors where the valence band maximum is energetically considerably lower than that of Si. A first option would be to employ p-type InP where efficient H₂ evolution has been observed [46] and where nanoemitter islands could be deposited onto the surface that has been photoelectrochemically passivated by an ultrathin interfacial layer [47, 48].

Basic interfacial chemistry analyzed by photoelectron spectroscopy

Figure 14 shows the Si 2p core level line recorded at BESSY II using our combined electrochemistry–UHV surface analysis system approach [49]. The spectrum was recorded after Pt deposition (Fig. 10) at 570 eV where the surface sensitivity, given by the inelastic mean free scattering length of the photoelectrons, is ~1.0 nm. The evaluation yields an oxide thickness of about 0.4 nm (using energy-dependent sensitivity factors of 1.7 for $\frac{I_{Si}}{I_{SiO_2}}$) which corresponds to about one ML. The energetic scheme in Fig. 15 shows that Pt deposition occurs in two steps as has been already mentioned above in “Solar devices”:

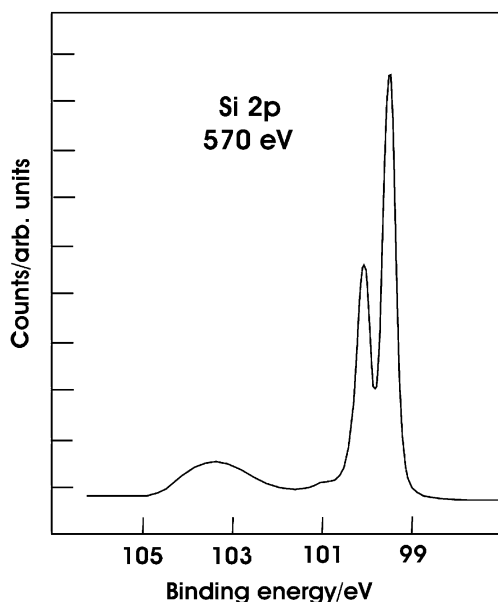
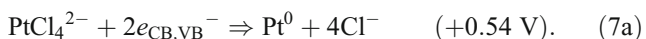
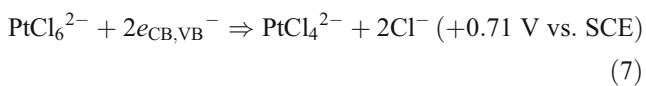


Fig. 14 Synchrotron radiation photoelectron data of the Si 2p line at an excitation energy of 570 eV; the signal at a binding energy of 103.7 eV is attributed to Si in SiO₂

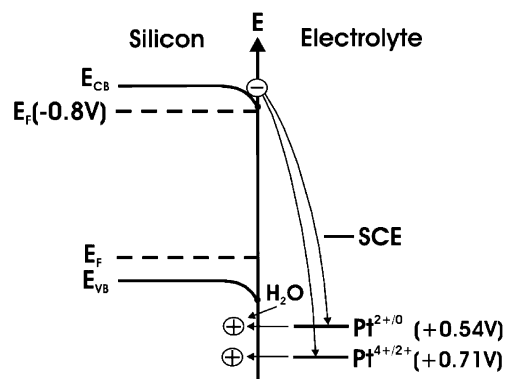


Fig. 15 Energy scheme for Pt deposition at the silicon–electrolyte interface; values for the work function of the normal hydrogen electrode (NHE) which locate that of the saturated calomel electrode (SCE) at 4.86 eV are taken from literature data and our data; the hole injection process in the presence of water is also indicated, resulting in silicon oxidation (see text)

The first step, the reduction of Pt⁴⁺ to Pt²⁺, precedes Pt deposition. The reduction can occur via conduction band electrons (index CB) or via valence band electrons. The XPS data in Fig. 14 show that a valence band process must be involved: By hole injection into the valence band, Si backbonds are weakened in the presence of water which results in solvolytic splitting of the backbonds and subsequent oxide formation as schematically shown in Fig. 15. Thereafter, the actual Pt deposition takes place. Electrodeposition from the conduction band occurs when the potential scan reaches –0.8 V. This deposition occurs at a stage in the process where Pt nuclei can have already been formed in the valence band process. As a consequence, a Pt/silicon oxide/Si contact is formed that has electronic properties similar to that of an MOS junction (see also part II). This explains the electronic behavior and, in particular, the absence of pronounced Fermi level pinning and results in the initially already rather good conversion efficiency of these first devices.

Conclusion and outlook

The preparation of photoactive devices prepared by low-temperature, scalable electrochemical processes that induce nanostructures in the passivating oxide on Si was shown. With Pt as nanoemitter material, photovoltaic as well as photoelectrocatalytic operation was observed. In the photovoltaic mode, efficiencies above 7% were obtained in a PECS using an iodine–iodide redox electrolyte.

Future work will address improvement of the electrodeposition process, better control of interface electronics at the respective metal–semiconductor junctions, oxide optimization, and the search for further suited candidates for electrodeposition that also function efficiently in solid-state

devices. In photoelectrocatalysis, the use of p-type semiconductors with low lying valence band edge for light-induced H₂ evolution and the use of other catalytically active noble metals is planned.

References

- Sze SM (1980) Semiconductor devices. Wiley, New York
- Turing AM (1952) Philos Trans R Soc Lond Ser B 237:37
- Kinoshita S, Yoshioka S, Kawagoe KK (2002) Proc R Soc London, Ser B 269:1417 doi:10.1098/rspb.2002.2019
- Mandelbrot BB (1982) The fractal geometry of nature. Freeman, New York
- de Tacconi MR, Chenthamarakshan CR, Yogeewaran G, Watcharenwong A, de Zoysa S, Basit NA et al (2006) J Phys Chem B 110:25347 doi:10.1021/jp064527v
- Lijima S (1991) Nature 354:56 doi:10.1038/354056a0
- Adachi E (2000) Langmuir 16:6460 doi:10.1021/la000244x
- Wehrspohn RB, Schilling J (2001) MRS Bull 26:623
- Li Y, Zheng M, Ma L, Shen W (2006) Nanotechnology 17:5101 doi:10.1088/0957-4484/17/20/010
- Teo SHG, Liu AQ, Singh J, Yu J, Sun HQ, Singh N (2006) Int J Nanosci 5:383 doi:10.1142/S0219581X06004516
- Cabrini S, Barsotti RJ, Carpentiero A, Businaro L, Zaccaria RP, Stellacci F et al (2005) J Vac Sci Technol B 25:2806 doi:10.1116/1.2062647
- Bundgaard E, Krebs FC (2007) Sol Energy Mater Sol Cells 91:1019 doi:10.1016/j.solmat.2007.01.013
- Su M, Fu L, Wu NQ, Aslam M, Dravid VP (2004) Appl Phys Lett 84:828 doi:10.1063/1.1645323
- Rauscher S (2004) PhD thesis, Brandenburgisch-Technische Universität Cottbus, Germany
- Lewerenz HJ, Aggour M, Murrell C, Kanis M, Jungblut H, Jakubowicz J et al (2003) J Electrochem Soc 150:E185 doi:10.1149/1.1542900
- Parkhutik V (2000) J Porous Mater 7:363 doi:10.1023/A:1009643206266
- Canham LT (1995) Adv Mater 7:1033 doi:10.1002/adma.19950071215
- Lewerenz HJ, Jakubowicz J, Jungblut H (2004) Electrochem Commun 6:460
- Skorupska K, Jakubowicz J, Jungblut H, Lewerenz HJ (2004) Superlattices Microstruct 36:211 doi:10.1016/j.spmi.2004.08.018
- Skorupska K, Lublow M, Kanis M, Jungblut H, Lewerenz HJ (2005) Appl Phys Lett 87:262101 doi:10.1063/1.2150267
- Skorupska K, Lublow M, Kanis M, Jungblut H, Lewerenz HJ (2005) Electrochem Commun 7:1077 doi:10.1016/j.elecom.2005.07.012
- Lewerenz HJ, Jungblut H, Rauscher S (2000) Electrochim Acta 45:4615 doi:10.1016/S0013-4686(00)00613-7
- Jungblut H, Lewerenz HJ (2000) Appl Surf Sci 168:194 doi:10.1016/S0169-4332(00)00589-4
- Grüning U, Lehmann V, Engelhardt C (1995) Appl Phys Lett 66:3254 doi:10.1063/1.113395
- Grzanna J, Lewerenz HJ, Jungblut H (2000) J Electroanal Chem 486:181–486:190
- Lewerenz HJ, Aggour M (1993) J Electroanal Chem 351:159 doi:10.1016/0022-0728(93)80231-6
- Lewerenz HJ, Schlichthörl G (1992) J Electroanal Chem 327:85 doi:10.1016/0022-0728(92)80138-T
- Grzanna J, Jungblut H, Lewerenz HJ (2005) AIP Conf Proc 780:635 doi:10.1063/1.2036832
- Skorupska K, Sadewasser S, Streicher F, Lewerenz HJ (2008) (in press)
- Skorupska K, Lublow M, Stempel T, Kanis M, Pettenkofer C, Lewerenz HJ (2008) (in press)
- Rappich J, Lewerenz HJ (1996) Thin Solid Films 276:25 doi:10.1016/0040-6090(95)08041-4
- Aggour M, Giersig M, Lewerenz HJ (1995) J Electroanal Chem 383:67 doi:10.1016/0022-0728(94)03723-G
- Sinton RA, Swanson RM (1987) IEEE Trans Electron Dev 34:2116 doi:10.1109/T-ED.1987.23205
- Lewerenz HJ (1997) J Phys Chem B 101:2421 doi:10.1021/jp962694x
- Markov AA (1971) Extension of the limit theorems of probability theory to a sum of variables connected in a chain (reprinted in Appendix B of: R. Howard: Dynamic probabilistic systems, vol 1: Markov chains). Wiley, New York
- Hong C, Akinwande AI (2005) Electrochem Solid-State Lett 8: F13 doi:10.1149/1.1887190
- Lublow M, Lewerenz HJ (2007) Electrochem Solid-State Lett 10: C51 doi:10.1149/1.2742503
- Grzanna J, Jungblut H, Lewerenz HJ (2007) Phys Status Solidi A 204:1245
- Carstensen J, Prange R, Popkirov GS, Föll H (1998) Appl Phys A 67:459 doi:10.1007/s003390050804
- Tersoff J (1984) Phys Rev Lett 52:465 doi:10.1103/PhysRevLett.52.465
- Yae S, Kitagaki M, Hagihara T, Miyoshi Y, Matsuda H, Parkinson BA et al (2001) Electrochim Acta 47:345 doi:10.1016/S0013-4686(01)00582-5
- Myland JC, Oldham KB (2004) Electrochem Commun 6:344 doi:10.1016/j.elecom.2004.01.013
- Kelly JJ, Vanmaekelbergh D (1998) Chapter 2 in: semiconductor micromachining vol. 1. In: Campbell SA, Lewerenz HJ (eds) Fundamental electrochemistry and physics. Wiley, Chichester
- van de Ven J, Kelly JJ (2001) J Electrochem Soc 148:G10 doi:10.1149/1.1344556
- Muñoz AG, Lewerenz HJ (2008) J Electrochem Soc 155:C527 doi:10.1149/1.2929834
- Heller A, Vadimsky RG (1981) Phys Rev Lett 46:1153 doi:10.1103/PhysRevLett.46.1153
- Lewerenz HJ, Schulte K (2002) Electrochim Acta 47:2633 doi:10.1016/S0013-4686(02)00125-1
- Schulte K, Lewerenz HJ (2002) Electrochim Acta 47:2639 doi:10.1016/S0013-4686(02)00124-X
- Lewerenz HJ (2008) Hothersall memorial award lecture. Trans Inst Metab Finish 86:19 doi:10.1179/174591908X264400